ELSEVIER

Contents lists available at ScienceDirect

Acta Biomaterialia

journal homepage: www.elsevier.com/locate/actbio



Full length article

Label-free structural and mechanical characterization of rat uterosacral ligaments

Joseph Thomas ^a, Kandace Donaldson ^{b,1}, Clara Gimenez ^{b,1}, Monique Vaughan ^c, Yizheng Zhu ^a, Raffaella De Vita ^b,*

- a Bradley Department of Electrical and Computer Engineering, Virginia Tech, 460 Turner Street, Suite 303, Blacksburg, 24061, VA, USA
- ^b STRETCH Lab, Virginia Tech, 330A Kelly Hall, 325 Stanger Street, Blacksburg, 24061, VA, USA
- e Pelvic Medicine and Reconstructive Surgery, University of Virginia, Fontaine Research Park Building, 500 Ray C. Hunt Drive, Charlottesville, 22903, VA, USA

ARTICLE INFO

Keywords: Uterosacral ligaments Uniaxial testing Optical coherence tomography Second harmonic generation Deformations Microstructure

ABSTRACT

This study presents quantitative applications of label-free imaging methods to characterize the structure of the uterosacral ligaments (USLs) before, during, and after loading. Rat USLs (n=14) were excised with their spinal and cervical attachments, clamped at these attachment sites, and pulled uniaxially in a custombuilt tensile testing machine along their main *in vivo* loading direction. During uniaxial testing, optical coherence tomography (OCT) images were recorded, revealing the re-arrangement and failure of the structural components of the USLs. Before and after uniaxial testing, second harmonic generation (SHG) microscopy was also used to image collagen and smooth muscle within the proximal, intermediate, and distal regions of the USLs. From the OCT images, two metrics, the global depth variation (GDV) and the bundle energy projection (BEP), were extracted to quantify morphological changes as a function of the applied load and displacement. The GDV metric measured the heterogeneity of the USLs, while the BEP metric quantified the re-orientation of fiber bundles under uniaxial testing. SHG images showed that the rat USLs have a complex microstructure with wavy collagen fibers interwoven with smooth muscle bundles. These findings on the structure-function relationship of USLs may have implications for developing non-invasive, label-free imaging modalities suitable for diagnosing conditions such as pelvic organ prolapse (POP) by evaluating the structural integrity of USLs.

Statement of Significance:

The uterosacral ligaments (USLs), often compromised in pelvic organ prolapse (POP), are the primary support to the uterus and vagina, yet surgeries to restore their function frequently have poor outcomes. Non-invasive diagnostic tools are needed to assess the integrity of the USLs for treatment planning and monitoring. This study examines how the morphology of the USLs changes under mechanical loading, using optical coherence tomography (OCT) for detailed three-dimensional imaging and quantitative optical parameters that correlate morphology with load. Complementary second harmonic generation (SHG) microscopy reveals the organization of smooth muscle and collagen within the tissue structure. These label-free imaging techniques may enable the real-time, noninvasive assessment of tissue integrity and hold potential for future applications in improving the diagnosis and treatment of POP.

1. Introduction

The uterosacral ligaments (USLs) are highly complex and fan-shaped structures that are essential for providing support to the uterus and apical vagina within the pelvic floor. These ligaments are concave in shape, connecting the cervix at their narrower distal ends to the sacral spine at their wider proximal ends. Their complex microstructure comprises multiple components, including collagen, elastin, smooth

muscle, blood vessels, lymphatics, and nerves [1,2]. These components are intertwined and layered in different three-dimensional orientations to form a thin, multi-layered tissue that contributes to the structural support and function of the pelvic region.

The USLs are generally conceptualized as having three anatomical regions in humans. The cervical/distal region consists mainly of densely organized smooth muscle bundles intertwined with densely packed connective tissue. The sacral/proximal region is almost entirely

E-mail address: devita@vt.edu (R. De Vita).

https://doi.org/10.1016/j.actbio.2025.08.009

Received 7 March 2025; Received in revised form 31 July 2025; Accepted 6 August 2025 Available online 27 August 2025

1742-7061/© 2025 Acta Materialia Inc. Published by Elsevier Inc. All rights are reserved, including those for text and data mining, AI training, and similar technologies.

^{*} Corresponding author.

¹ These authors contributed equally to this work.

composed of loosely organized connective tissue with little smooth muscle. The intermediate region spans the other two and encompasses the gradual transition from tightly packed and predominantly muscular tissue to loosely disordered collagenous tissue [1,2]. These differences in components and their relative organization likely determine the USLs' supportive function in the body.

Structural changes of the USLs have been shown to contribute to the development of pelvic organ prolapse (POP). Pelvic organ prolapse is a major public health concern in the United States, affecting 50% of women who give birth [3]. It is a condition characterized by the descent of pelvic organs such as the uterus, bladder, rectum, or vaginal apex from their usual anatomical positions into or outside the vaginal canal. Given their anatomical function, the USLs are used as anchoring tissues in surgical procedures for POP, such as the USL vaginal vault suspension [4]. Thus, characterizing the mechanical function of the USLs, particularly in vivo, is important not only for identifying the etiology of POP but for improving corrective surgeries that rely on the USLs to restore the support of prolapsed organs. To date, no in vivo measurement technologies exist to evaluate the USL integrity, and their development could be transformative, improving diagnosis, treatment personalization, surgical efficacy, and research progress in pelvic floor health. Optical imaging can offer "optical biopsy" with some of the most desirable features, such as non-invasiveness and endoscopy compatibility. Although optical techniques have not yet been established as reliable tools for quantifying the USL mechanical integrity, an early ex vivo study by the authors using OCT on swine models has shown promising potential in this area [5].

Animal models can help study the functional role of the USLs in POP through *ex vivo* mechanical testing, bypassing the challenges associated with human tissue collection [6,7]. Large animal models, in particular, present several advantages over small animal models due to the larger size of their USLs, which facilitates the collection of multiple specimens from a single animal [5,6,8–10]. Recently, we developed experimental methods for isolating and mechanically testing rat USLs, which, although small, are relatively easy to acquire, cost-effective, and histologically similar to human USLs, making them a practical choice for controlled experimental studies [11].

In a comparative study published on the anatomy and histology of the human, rat, and mouse USLs, Iwanaga et al. [12] determined that rat USLs had the same insertion sites as human USLs, with the proximal connections originating from the S2-S4 region of the sacral vertebrae and the distal connections occurring at the cervix where they were contiguous with the cardinal ligaments. In the distal region, the USL contained densely packed smooth muscle fascicles, abundant blood vessels, and small nerve bundles. The mid portion was primarily composed of strands of connective tissue and collagen with fewer smooth muscle bundles and vascular structures. The proximal portion consisted mostly of loose strands of connective tissue and collagen with minimal vessels and nerves. They also found that collagen and smooth muscle content were similar in human and rat distal USLs (50% vs. 70% and 36% vs. 27%, respectively). Despite these similarities and the advantages that would be afforded by establishing the rat as an animal model for studying the USLs (i.e., controlled conditions, such as pregnancy, parity, disease, and age, and low housing, veterinary, and research costs), there have been only a few studies on their mechanical properties [13,14]. Moalli et al. [13] and Lowder et al. [14] tested the rat USLs together with the vagina by fixing the spine and pulling the vagina caudally until failure. More recently, Miller et al. [15] utilized a rat model to evaluate a fibrous hydrogel designed to strengthen the USLs as a treatment for POP. The cited studies reported mechanical results based on testing the USLs together with other pelvic tissues, not in isolation.

Our group has recently performed *ex vivo* uniaxial tensile tests of rat USLs after isolating the ligaments from their surrounding tissues and organs [11]. The USLs were pulled along their main *in vivo* loading directions, with clamps at the cervical and spinal attachments. The

deformations of the USLs were measured by tracking the displacement of speckles applied to the surface of the specimens using a non-contact optical technique, the digital image correlation (DIC) method. We have also observed that rat USLs fail through delamination, making the DIC method insufficient for fully capturing their complex deformations. This limitation arises not only because DIC assumes continuous strain fields, which cannot account for localized structural changes (e.g., collagen fiber failure, smooth muscle bundle rupture, or delamination of these components), but also because DIC measures only surface strain, and cannot capture the full-depth deformations occurring within the tissue. Complementary imaging techniques are needed to fully describe the *ex vivo* complex deformation and failure mechanisms of the USLs throughout their entire loading range.

Optical coherence tomography (OCT), along with other non-optical tomographic techniques [16,17], has been widely used to study the three-dimensional morphology of soft tissues and their relevant biomechanical properties. OCT is label-free and non-invasive, using the amplitude of back-scattered light as endogenous contrast and its time of flight to determine the depth of the tissue structures. In mechanical studies of soft tissues, OCT has been employed *ex vivo* to measure the thickness of thin and transparent specimens during testing [18], calculate strain in specimens subjected to small deformations [19–21], and characterize the three-dimensional morphology of excised [22] and cultured [23] tissues. OCT has also been used broadly in clinical applications for *in vivo* imaging of the eye in response to changes in intraocular pressure [21] and single-shot diagnoses [24].

Due to its depth-resolving imaging capabilities, OCT is a promising imaging technique for studying the deformations of rat USLs as they approach failure. The two primary functional modes of OCT for quantifying soft tissue deformation are digital volume correlation (DVC) and optical coherence elastography (OCE). DVC is an image-based technique to calculate displacements and strain fields from static tomographic images (e.g., pre- and post-deformation images). This method has been applied to both *ex vivo* [25] and *in vivo* studies of deformation [20,26,27]. In contrast, OCE employs a mechanical perturbation to the sample, typically as an air puff, followed by a real-time measurement of the tissue's mechanical response using OCT. OCE has been successfully applied to characterize the intrinsic mechanical parameters of tissues *ex vivo* [28–31] and *in vivo* [32]. Both DVC and OCE are primarily suited for analyzing small to moderate deformations.

A significant gap exists in the current analysis methods for OCT techniques when capturing extreme deformations in specimens loaded to failure, such as the rat USLs. For DVC, accurate strain field mapping requires smooth, continuous specimen deformation. However, near failure, tissues often exhibit irregular or discontinuous displacements, disrupting DVC's ability to track and quantify strain fields reliably. Similarly, DIC, the surface-based counterpart to DVC, faces analogous limitations in these scenarios. OCE encounters additional challenges under static or quasi-static loading conditions, such as uniaxial mechanical testing, where elastic waves are not generated. In these cases, strain at a specific image point depends not only on the local tissue mechanics (as it does for propagating elastic waves) but also on the global surrounding deformation of the entire specimen [33]. This interdependence complicates the analysis of tissues undergoing large-scale deformation near failure. To address these limitations, new analysis tools for optical tomography are needed to study specimens approaching failure, such as the rat USL during ex vivo uniaxial loading and, more importantly, the in vivo compromised support of USLs in POP

OCT provides high-resolution imaging of tissue, typically on the scale of a few micrometers. However, it lacks the molecular specificity required to identify or analyze individual tissue components (e.g., collagen, smooth muscles). Second harmonic generation (SHG) bridges this gap by enabling sub-micron resolution imaging with the molecular specificity necessary for visualizing some structural proteins in reproductive tissues. While no publications to date report SHG

studies of USLs, several researchers have demonstrated the utility of SHG in examining the collagen content in reproductive tissues. SHG microscopy has been used to image the cervix in humans and rodents, revealing differences in collagen organization at various pregnancy stages [34,35] and between pre- and post-menopause [36]. Further research has highlighted correlations between the collagen microstructure and the mechanical properties of cervical and vaginal tissues in various animal models [37–39]. Importantly, SHG imaging is compatible with endoscopy, enabling non-invasive, *in vivo* optical biopsies. For example, fiber-optic micro-endoscopes have been successfully used in live animal models to monitor cervical remodeling during pregnancy and evaluate kidney functions in real-time [40,41].

This study presents the application of OCT and SHG microscopy to characterize the microstructure of the rat USLs before, during, and after uniaxial tensile testing. Label-free parameters derived from OCT data are introduced to quantify the three-dimensional morphological changes in the USLs throughout the entire loading regime, encompassing the toe, linear, and failure regions of the load-displacement curve. SHG microscopy is used to image collagen and smooth muscle in the proximal, intermediate, and distal regions of the USLs before and after uniaxial tensile testing, revealing their region-specific organization. The combined use of OCT and SHG, two complementary label-free imaging techniques with demonstrated endoscopic capability, allows for multiscale characterization of USLs, as these imaging methods operate at different length scales and provide distinct yet complementary information. This work not only advances our understanding of the structural and mechanical support function of USLs but also introduces imagebased metrics that may serve as the foundation for the development of non-invasive optical probes for the clinical prevention, diagnosis, and surgical treatment of POP.

2. Materials and methods

2.1. Specimen preparation

This study was conducted with approval from the Institutional Animal Care and Use Committee (IACUC) at Virginia Tech. A total of 14 virgin Sprague-Dawley rats, aged 13-14 weeks, were used in this study. The rats were euthanized via decapitation and stored at -20 °C. They were thawed at 4 °C for 2-4 days and further thawed at room temperature (20-25 °C) for 2-3 h on the days of the experiments. The USLs were excised from the rats using a dissection technique that preserved the proximal and distal attachments of the ligaments as described elsewhere [11]. Phosphate buffered saline (PBS) was applied to the specimens intermittently throughout the dissection to keep them hydrated. The thickness of each specimen was measured using a CCD laser displacement sensor (LK-G82, Keyence, Inc., Japan) at nine random points within the USL, three in each of the proximal, intermediate, and distal anatomical regions, which was defined as equal thirds of the total USLs. These regions were identified by eye based on specimen thickness, anatomical landmarks, and location, but this distinction was approximate. Measurements of the specimen clamp-to-clamp length, width, and thickness in each region were collected in triplicate using ImageJ (NIH, Bethesda, MD). The thickness and width measurements were averaged in each region and reported in Table 1. All n = 14specimens were subjected to mechanical testing with concurrent OCT imaging. Moreover, before and after mechanical testing, a subset of the specimens (n = 8 out of 14) were imaged using SHG to visualize smooth muscle and collagen fibers.

2.2. Mechanical testing

The mechanical testing methods are presented in detail in a recent publication by Donaldson and De Vita [11]. Custom 3D printed L-shaped clamps were used to mount the specimens for testing; a vise-style clamp with ridged surfaces was used to grip the spine at

Table 1 Mean (\pm standard deviation (S.D.)) thicknesses and widths of the USL specimens in their three anatomical regions (n=14). The mean clampto-clamp length for the specimens was 17.2 \pm 2.9 mm.

1 0	_	
Region	Thickness (mm)	Width (mm)
Proximal	4.24 ± 0.43	17.10 ± 2.16
Intermediate	3.43 ± 0.53	13.78 ± 1.68
Distal	2.54 ± 0.50	13.74 ± 1.69

the proximal/sacral end, and a block holding three L-shaped needles spaced 3.5 mm apart was used to puncture through the cervical/vaginal attachments (Fig. 1(a)). The specimens were then tested using a custom-built tensile testing apparatus, which consisted of one 8.9 Ncapacity load cell with 0.1% accuracy (FSH00092, Futek Advanced Sensor Technology, Inc., Irvine, CA), two linear actuators with a maximum stroke length of 25 mm and 0.048 µm micro-step size resolution (T-NA08A25, Zaber Technologies, Inc., Vancouver, BC, Canada), and an acrylic tissue bath filled with PBS. The USLs were pulled to an initial load of 5 mN at a rate of 15 $\mu m/s$ to ensure that specimens were relatively flat and unfolded before the test. The displacement at this 5 mN preload was defined as the reference configuration, providing a standardized starting point for all mechanical tests. Then the USLs were pulled at 10 μ m/s in the main *in vivo* loading direction (the *x*-direction in Fig. 1(a)-(b)) until the actuators reached their maximum stroke lengths. Mechanical testing protocols were programmed in LabVIEW (NI, Austin, TX).

The displacement values at the transition points of the typical three regions, toe, linear, and failure regions, of the load–displacement data were identified using MATLAB (R2023b; The MathWorks, Inc., Natick, MA, USA). The displacement value at the transition between toe and linear regions was computed semi-automatically using the *ischange* function with a linear fitting method. This method found the point in the load–displacement curve where the slope of a linear fit changes, segmenting the load curve into two regions based on a cost function [42]. The displacement value at the transition between the linear and failure regions was at the maximum load.

2.3. OCT imaging system and protocol

A spectral domain optical coherence tomography system (SD-OCT) was used to capture through-thickness images of the intermediate regions of the rat USLs during tensile testing as this region was thinner and located away from the clamps, minimizing imaging artifacts and mechanical disturbances (Fig. 1(b)). The system was assembled with a superluminescent diode (SLD; Superlum, Cork, Ireland; $\lambda = 837$ nm, $\Delta \lambda = 54$ nm) and a custom spectrometer using a linescan camera (AViiVA EM1; Teledyne, Milpitas, CA; 1024 pixel, 78 kHz). It was mounted above the specimen, maintaining a working distance of 150 mm. It provided a lateral resolution of 60 µm. For volume acquisition, the optical beam was raster scanned with a 12 µs dwell time in the xand y- directions (Fig. 1) across a field of view (FOV) of 7.5 mm \times 15 mm area with a 512×512 image size. The imaging range in the depth direction, the z- direction, was approximately 3 mm in 513 image pixels. Thus, each recorded OCT volume was $512 \times 512 \times 513$ voxels in the $x \times y \times z$ directions of size 7.5 mm \times 15 mm \times 3 mm. Each voxel measured approximately 14.6 μm , 29.3 μm , and 5.85 μm in the x-, y-, and z- direction, respectively. Depth measurements represent optical depths, calculated as the physical distance multiplied by the refractive index of the sample medium. Measured depths in water (refractive index \sim 1.3) and tissue (refractive index \sim 1.4) are approximately 1.3 to 1.4 times greater than their equivalent optical path length in air (refractive index ~1.0). For each specimen, 30 to 40 OCT volumes were captured during uniaxial testing, while color images were recorded simultaneously with a CMOS camera (Sony ILCE-7M2 camera with Sony FE 28-70 mm F3.5-5.6 OSS lens, Sony Corporation, Tokyo, Japan). Each OCT volume required approximately 3-4 s to

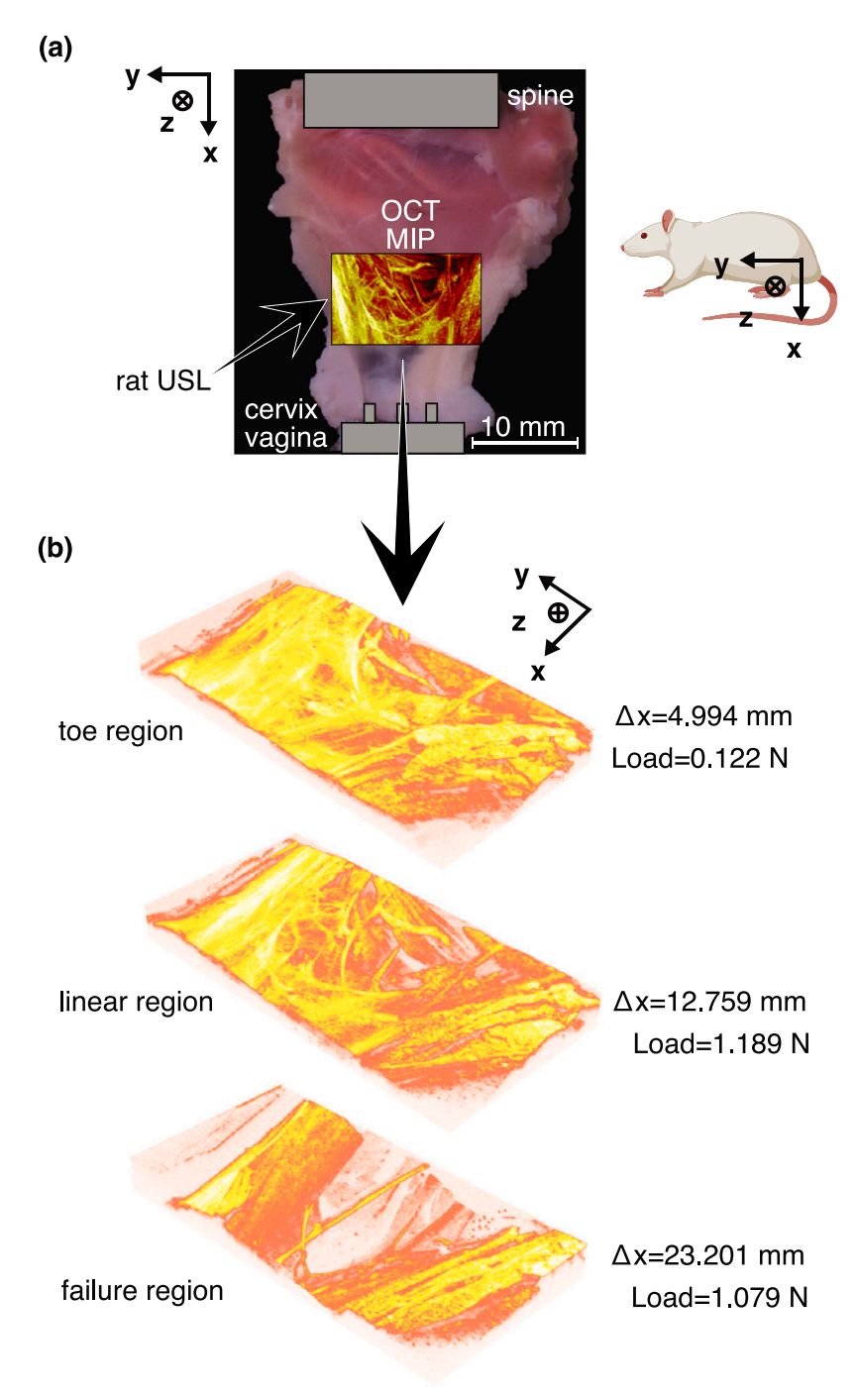


Fig. 1. (a) Picture of a rat USL specimen loaded along the main *in vivo* loading direction, the x-direction, with the OCT maximum intensity projection (MIP) overlay. The specimen, which is clamped between the cervix/vagina and spine, is under a load of 1.189 N and at a displacement, Δx , of 12.759 mm. (b) Isometric OCT MIP images at displacements, Δx , and loads that fall within the toe, linear, failure regions of the load-displacement curve.

capture. OCT images were acquired intermittently every 30 s to 1 min throughout testing, without pre-alignment to specific displacement increments. The OCT and mechanical testing programs were started simultaneously, and timestamps were used to align the OCT images with the corresponding load and displacement data. The actuator displacement during each OCT scan ($\sim\!40~\mu m$) was smaller than the OCT system's resolution ($\sim\!60~\mu m$), so motion during imaging was negligible. Fig. 1(a) illustrates a representative USL, with panel (a) showing a color image of the specimen mounted in the testing apparatus overlaid with the corresponding OCT image, and panel (b) displaying isometric OCT reconstructions for load and displacement values across the three regions of the load–displacement curves for the same specimen.

2.3.1. Global depth variation for tissue heterogeneity

To quantify tissue heterogeneity (i.e., layered structure and the presence of diferent tissue components) under the extreme deformations observed when loading USL specimens to failure, we introduced a scalar parameter called global depth variation (GDV). GDV was calculated for every OCT volume acquired during uniaxial tensile testing as the displacement increased.

First, we generated 2D images using maximum intensity projection (MIP) along the depth (through-thickness) direction, the z-direction, of the 3D OCT volume. This projection identifies the brightest intensity point at each depth and maps it onto the x-y (en face) plane. Each pixel in the resulting 2D MIP image retains an associated depth value,

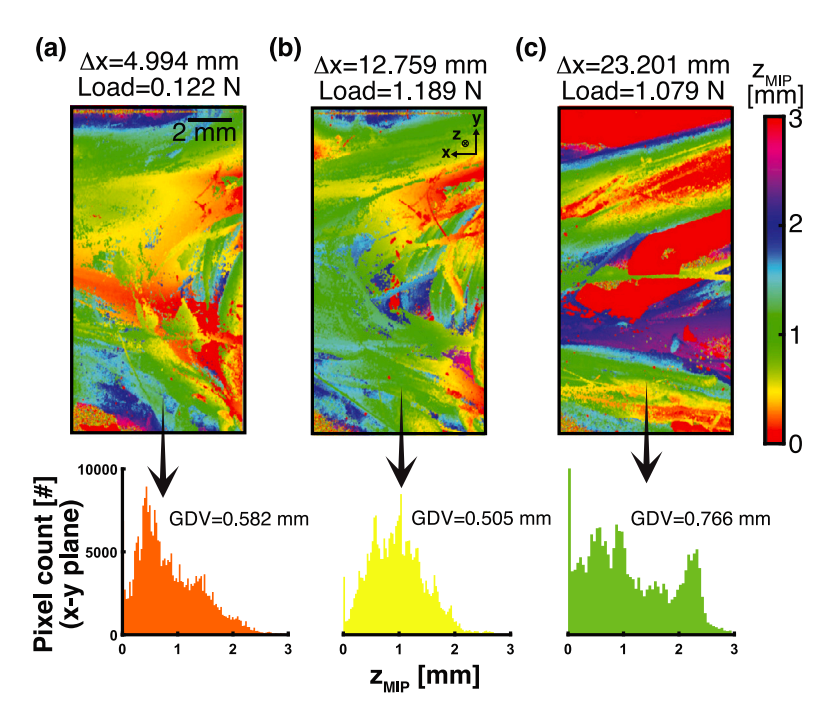


Fig. 2. Depth-encoded z_{MIP} images for one representative USL specimen in (a) the toe region, (b) the linear region, and (c) the failure region of the load–displacement curve. The coordinate $z_{MIP} = 0$ denotes the uppermost surface of the specimen, with increasing z_{MIP} values indicating greater depths within the tissue. The corresponding pixel count distributions of z_{MIP} are shown below each image, along with the calculated GDV values. The GDV is lower in the toe and linear regions, where structural heterogeneity is reduced (for example, features are concentrated within a narrow depth range), and higher in the failure region, where depth heterogeneity increases due to local structural changes (such as feature displacement, separation, or reorganization across depths).

 $z_{MIP}(x,y;\Delta x)$, representing the location of the brightest intensity point along the depth direction at the (x,y) point (associated with a pixel) at a given displacement Δx .

In the second processing step, a mask was applied to the MIP image to exclude off-tissue regions, ensuring that only depth values corresponding to the tissue were used. This step prevented irrelevant data, such as background noise, from skewing the calculations. After masking, the GDV was defined at a displacement Δx as the root-mean-square deviation of the depth values in the MIP image:

$$GDV(\Delta x) = \sqrt{\frac{1}{N} \sum_{(x,y)} (z_{MIP}(x,y;\Delta x) - \bar{z}_{MIP}(\Delta x))^2}$$
 (1)

where $z_{MIP}(x, y; \Delta x)$ denotes the depth value of the (x, y) point (corresponding to a pixel) in the MIP (filtered) image, \bar{z}_{MIP} represents the mean depth value across all pixels in such image, and N is the total number of (x, y) points (or pixels) in the image. Subtracting the mean depth, \bar{z}_{MIP} , in Eq. (1) ensured that the RMSD reflected the spread of depth values relative to the mean, effectively ignoring the bulk vertical movement of the tissue during testing. Fig. 2 illustrates depth-encoded MIP images for a representative specimen at three distinct points along the load-displacement curve, corresponding to the toe, linear, and failure regions. These images capture how the spatial distribution and depth variability of prominent features evolve throughout the loading process and also present the corresponding GDV values, which quantify the structural heterogeneity at each stage. The distributions of depth values differ across the regions: in the toe and linear regions, depth values are more tightly clustered, indicating lower heterogeneity, while in the failure region, the distribution broadens significantly, reflecting increased variability and greater depth heterogeneity consistent with localized structural changes.

Fig. 3 reports the GDV as the displacement and load increased for a representative specimen. The load-displacement curve can be divided into three regions: an initial fast-rising toe region, followed by a near-linear elastic region, and a prolonged non-linear failure region. The displacements at the transition points shown in Fig. 1(b) and Fig. 2

are marked in Fig. 3. The GDV quantifies the depth-wise heterogeneity of morphological features within the specimen. Specifically, GDV measures the variability in the depth locations of the most prominent features across the USL specimen, as derived from the MIP image. A larger GDV indicates that these features are distributed across a broader range of depths, reflecting greater structural heterogeneity. Conversely, a smaller GDV suggests that significant features are concentrated near a common depth, with minimal variation across the USL specimen. This interpretation is consistent with the observed trends: GDV decreases during the toe region, where tissue compaction reduces depth variability; it remains relatively constant in the linear region due to minimal through-thickness changes; and it increases in the failure region as tissue's breakage introduces new depth variations.

2.3.2. Bundles energy projection for realignment

To quantify the reorientation of USL collagen fiber bundles and smooth muscle bundles under uniaxial tensile loading, we introduced the bundle energy projection (BEP). BEP measures the proportion of energy (signal intensity) as projected onto specific planes, reflecting the global alignment of bundles. Changes in BEP as the displacement (and the load) increased were analyzed as a relative change, providing a robust metric for assessing structural realignment.

To begin the analysis, OCT volumes were processed to enhance the visibility and representation of collagen fiber bundles and smooth muscle bundles. The first step involved rescaling the OCT images to ensure isotropic voxel dimensions, providing uniform resolution in all three spatial directions. Following this, a 3D multiscale vessel enhancement filter, the Frangi vesselness filter [43], was applied using MATLAB's *fibermetric* function. This filter isolated tubular structures approximately 500 μ m in diameter (~30 voxels), highlighting bundles while suppressing noise and irrelevant structures. The resulting filtered images, $i(x, y, z; \Delta x)$, at a displacement Δx represented the energy (signal intensity) of detected bundles in the 3D volume, forming the foundation for subsequent analysis.

MIPs of $i(x, y, z; \Delta x)$ onto three orthogonal planes were then calculated. These were denoted as $i_{MIP}(x, y; \Delta x)$ for the *en face* projection,

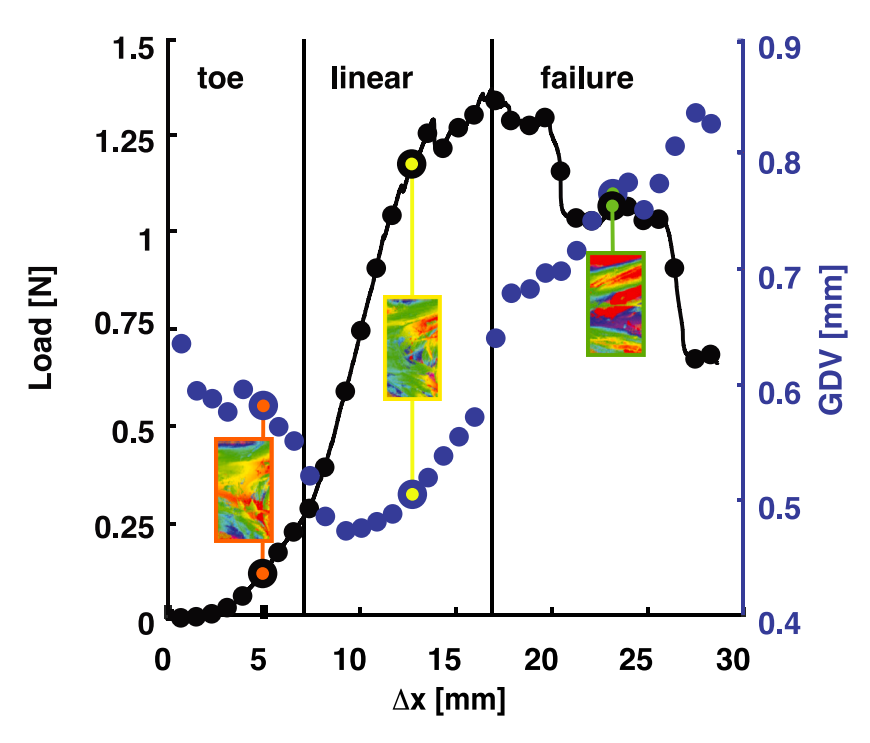


Fig. 3. Load-displacement curve with corresponding computed GDV for one representative USL specimen in the toe, linear, and failure regions. Load, displacement, and GDV values that are associated with images in Fig. 2 are marked.

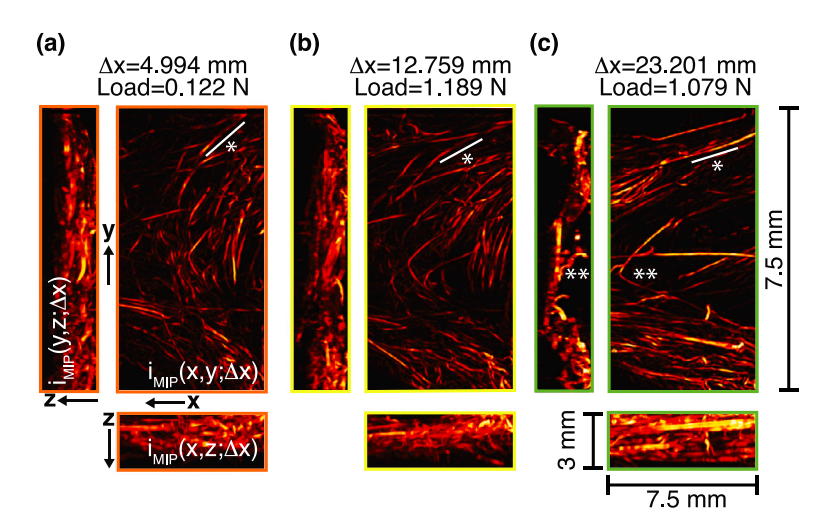


Fig. 4. Maximum intensity projections, $i_{MIP}(x, y; \Delta x)$, $i_{MIP}(y, z; \Delta x)$, and $i_{MIP}(x, z; \Delta x)$ of a filtered image with intensity $i(x, y, z; \Delta x)$ for a representative USL specimen (intermediate region) at three load–displacement values reported in (a), (b), and (c). Tensile loading is applied in the x-direction. Collagen and smooth muscle bundles realigned as the load increased (*) and some disappeared due to breakage (**).

 $i_{MIP}(y,z;\Delta x)$ for the transverse projection, and $i_{MIP}(z,x;\Delta x)$ for the longitudinal projection. These MIPs captured the energy distribution on each plane, reflecting bundle alignment relative to the loading direction. For instance, the alignment of bundles with the x-y plane increased the value of $i_{MIP}(x,y;\Delta x)$ while misalignment reduced such intensity in this plane. Fig. 4 shows MIP images for a representative volume after rescaling and filtering at different load–displacement stages.

BEP quantified the proportion of energy in each MIP relative to the total energy in the 3D image volume. For example, the BEP for the x-y plane at a given displacement Δx was calculated as:

$$BEP_{x-y}(\Delta x) = \frac{\sum_{(x,y)} i_{MIP}(x,y;\Delta x)}{\sum_{(x,y,z)} i(x,y,z;\Delta x)},$$
 (2)

where $\sum_{(x,y)}$ denotes the sum of intensity values across all pixels in the x-y plane and $\sum_{(x,y,z)}$ denotes the sum of intensity values across all

voxels in the 3D volume. Similar calculations were performed for the y-z and x-z planes to obtain BEP_{y-z} and BEP_{x-z} . These quantities were computed for each OCT volume collected during tensile testing as Δx increased.

The BEP relative change, denoted by e, was used to quantify the reorientation of fibers during uniaxial tensile testing. This quantity compared the normalized energy in each projection plane at a given applied displacement Δx to its value at the start of testing (i.e., $\Delta x = 0$). For the x-y plane, the relative change was calculated as:

$$e_{x-y}(\Delta x) = \frac{BEP_{x-y}(\Delta x) - BEP_{x-y}(0)}{BEP_{x-y}(0)} \,. \tag{3}$$

Similarly, e_{y-z} and e_{x-z} were calculated for the y-z and x-z planes, respectively.

Fig. 5 illustrates these relative changes for a representative specimen across all three planes. The x - y projection (*en face*) showed minimal

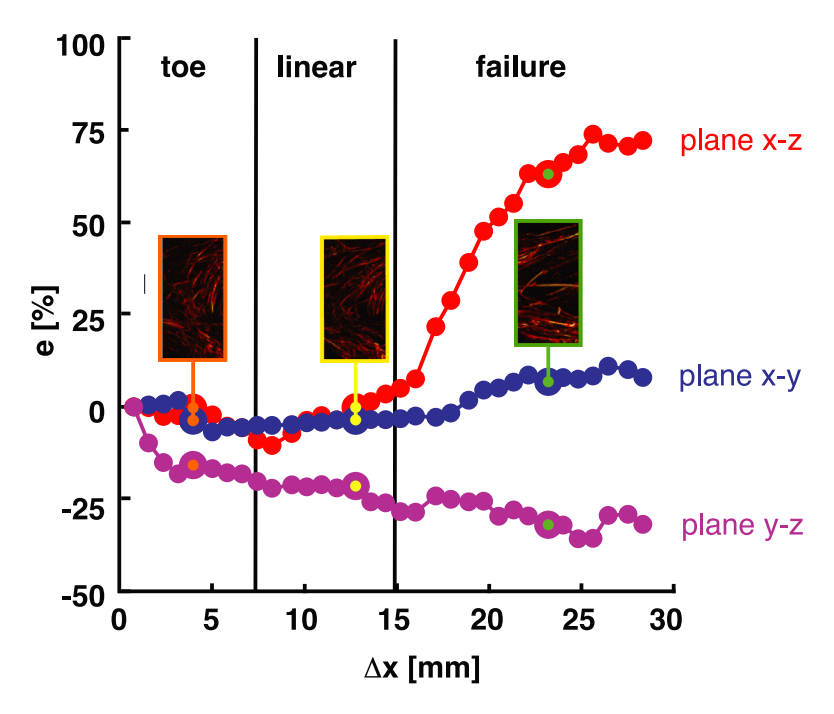


Fig. 5. Relative changes, e_{x-y} , e_{y-z} , and e_{x-z} of BEP in the three orthogonal planes for a representative USL specimen in the toe, linear, and failure regions. The BEP of load-displacement points of Fig. 4 are marked.

change for thin tissue such as the USL due to limited changes in the out-of-plane alignment during loading. However, e_{y-z} decreased, reflecting reduced alignment in the transverse plane, and e_{x-z} increased, indicating realignment along the loading direction.

This behavior can be understood by considering how bundle orientation directly affects the energy projections, which are quantified by the BEP values in each plane. For example, a bundle initially oriented diagonally in the x-y plane will contribute a higher intensity to $i_{\text{MIP}}(x, y; \Delta x)$, which increases the numerator in the calculation of $BEP_{x-y}(\Delta x)$. As the bundle reorients towards the loading direction (along the x-axis), its projection onto the x-z plane increases, meaning $i_{\text{MIP}}(z, x; \Delta x)$ becomes larger, increasing $BEP_{x-z}(\Delta x)$. Simultaneously, the projection onto the y-z plane decreases, reducing $i_{MIP}(y,z;\Delta x)$ and thus $BEP_{v-z}(\Delta x)$. Alternatively, a bundle initially aligned along the z-axis will have minimal projection onto the x-y plane, resulting in a smaller $BEP_{x-y}(\Delta x)$, while its projections onto the y-z and x-z planes (and thus $BEP_{v-z}(\Delta x)$ and $BEP_{x-z}(\Delta x)$) will be more significant. If the bundle remains vertical during loading, these BEP values will remain relatively constant. The relative change in BEP, e, then quantifies these shifts as the displacement increases. For example, as the bundle's projection onto the x-z plane increases, $BEP_{x-z}(\Delta x)$ increases relative to its initial value $BEP_{x-z}(0)$, producing a positive $e_{x-z}(\Delta x)$. Conversely, as projections decrease in the y-z plane, $e_{v-z}(\Delta x)$ becomes negative.

2.4. Second harmonic generation imaging

Before and after mechanical testing, n=8 of the 14 specimens were imaged using SHG to visualize their smooth muscle and collagen fibers, the most plentiful structural component of the USLs [44]. Each specimen was arranged in a shallow well filled with PBS within a petri dish. A glass cover slip was placed over each specimen so that the top surface (the medial anatomical surface of the USL) was in contact with the slip and, therefore, in one smooth plane. The dish was placed on the motorized stage of a Zeiss LSM 880 upright multiphoton confocal microscope (Zeiss, Thornwood, NY). Backward-SHG imaging was performed with a Ti:Sapphire laser producing 140 fs pulses with a laser wavelength set at 780 nm and an 80 MHz repetition rate (Ultra 1, Coherent Inc., Santa Clara, CA). The laser power was adjusted

based on the imaged region: lower power was used for collagen-rich areas, while higher power was necessary to visualize smooth muscle bundles due to their weaker SHG signal. Using a 20 xdry objective lens with an effective numerical aperture of 0.8, two-dimensional images (425.10 \times 425.10 μm^2 , 1024 \times 1024 pixels) were acquired at various points in the tissue specimens and in each of the distal, intermediate, and proximal USL regions. This regional distinction was approximate, based on visual inspection, specimen thickness, and anatomical landmarks. The points and depths at which the images were taken were selected according to the highest visibility of collagen and muscle while panning around each USL region. The number of images taken for each specimen was limited by time, as total imaging time was kept to 1–1.5 h to keep the tissue fresh.

2.5. Statistical methods

Statistical comparisons were performed using JMP statistical software (Version 18.0.2, SAS Institute Inc., Cary, NC). Significance was set at p < 0.05. A one-way factorial repeated-measures ANOVA was conducted to assess the effect of mechanical region (toe, linear, and failure) on the mean values of GDV. The means were computed across the regions. The analysis met the required assumptions of normality of the response distributions within each factor level, homogeneity of variances across factor levels, and independence of observations. To identify differences between individual mechanical regions, post hoc comparisons were performed using Tukey's Honest Significant Difference (HSD) method. For BEP relative changes, e, the Shapiro-Wilk test indicated that mean values were not normally distributed (p < 0.001). However, according to the Central Limit Theorem, the sampling distribution of estimates approaches normality as sample size increases. While the suggested range for the sample size varies, slight deviations from normality are generally acceptable for smaller sample sizes [45,46]. In this study, residuals exhibited only modest deviations from normality, allowing for a relaxation of the normality assumption. All other statistical assumptions were satisfied. A two-way factorial repeated-measures ANOVA was conducted to evaluate the effects of mechanical region (toe, linear, and failure) and plane (x - y, y - z,and x - z) on the mean values of the BEP relative changes. The main effects of each factor and the interaction between region and plane

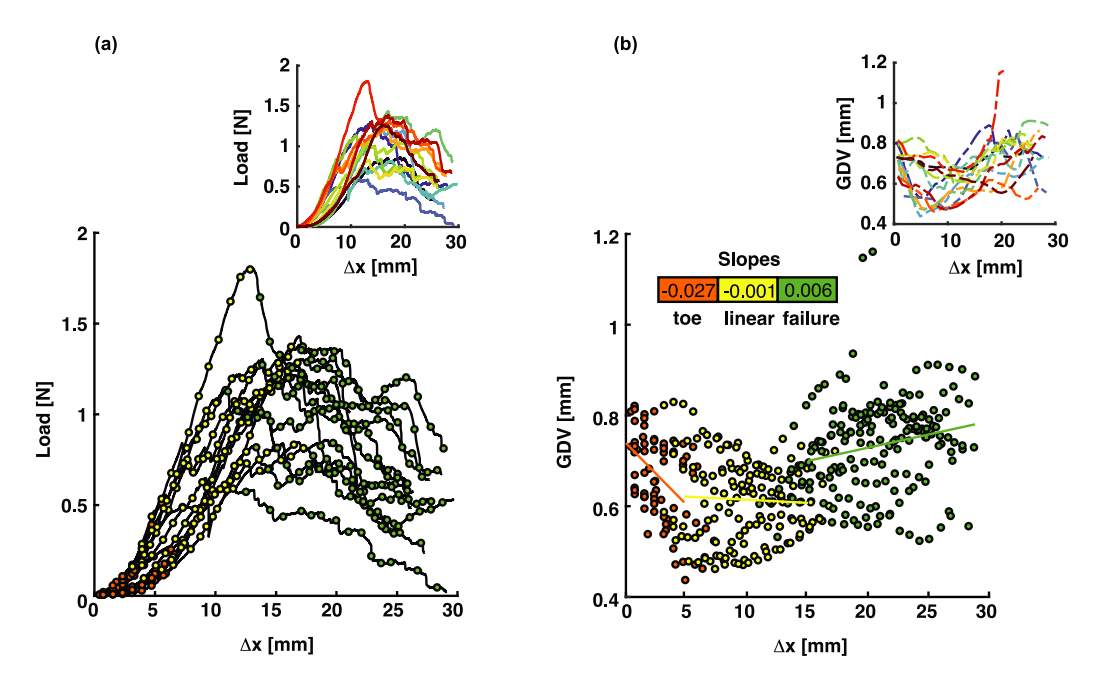


Fig. 6. (a) Load *versus* displacement data and (b) the corresponding GDV *versus* displacement data for USLs (n = 14). In the inserts, data from the same specimens are reported in the same color in (a) and (b). Data in (a) and (b) are clustered by toe (orange circles), linear (yellow circles), and failure (green circles) regions. A linear fit was applied to GDV *versus* displacement data within each load region and the slopes in each region are also reported. Across all specimens, the GDV decreased in the toe region of the load–displacement curve, remained slowly varying in the linear region, and increased in the failure region. Data in (b) for (n = 14) specimens illustrates the amount of OCT data collected for this study, where one GDV point is computed from each OCT volume. These 409 computed GDV points represent 165 GB of OCT volume data.

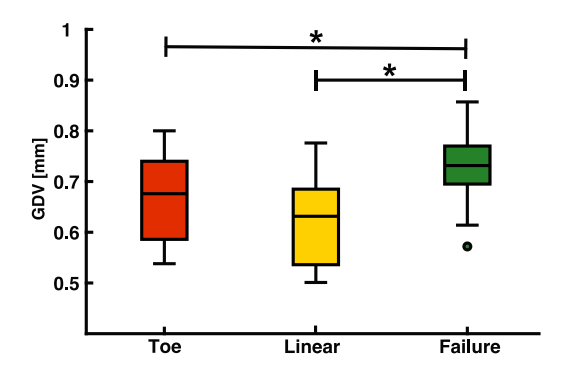


Fig. 7. Boxplot of GDV values (means across each region) in the toe (orange), linear (yellow), and failure (green) regions for USLs (n=14). Mean GDV value in the failure region was significantly different than the mean GDV in the toe region and linear regions (*, p < 0.05).

were analyzed. When a significant interaction was observed (p <0.05), post hoc analyses were performed using Tukey's HSD test to determine specific pairwise differences between region-plane combinations.

3. Results

3.1. Load-displacement data

Fig. 6(a) presents load *versus* displacement data measured during tensile testing for the n=14 specimens. While there was appreciable inter-specimen variability among the data, each tested specimen exhibited a nonlinear behavior characterized by an initial low-stiffness toe region, a subsequent high-stiffness linear region, and a final region of gradually decreasing stiffness. Table 2 lists the mean (\pm S.D.) moduli and maximum loads achieved by the USLs during mechanical testing. In Fig. 6(a), these three distinct regions, the toe, linear, and failure regions, of the same curves are presented as determined by the computed transition displacements. The transition displacements from the

Table 2 Mean (\pm S.D.) values for secant and tangent stiffness, maximum load, and displacement at maximum load (n = 14).

and displacement at maximum load (n = 14).			
Mechanical parameter	Mean \pm S.D.		
Secant Stiffness (N/mm)	0.040 ± 0.018		
Tangent Stiffness (N/mm)	0.13 ± 0.04		
Maximum Load (N)	1.16 ± 0.31		
Displacement (mm) at Maximum Load	15.0 ± 2.5		

toe-to-linear and linear-to-failure regions, computed individually for each specimen, occurred at different displacements for each sample. The mean (\pm S.D.) toe-to-linear displacement was 4.8 \pm 1.7 mm, while the mean linear-to-failure displacement was 15.0 \pm 2.5 mm. Grouping all n=14 specimens by the three regions (i.e., toe, linear, and failure regions) enabled a collective analysis of OCT-derived parameters since these parameters were computed across specimens in each load–displacement region.

3.2. OCT-derived data: GDV and BEP

During mechanical testing, OCT 3D volume scans revealed that the collagen and smooth muscle bundles were initially oriented in various directions and displayed varying degrees of waviness, showing a non-uniform structural organization. As the applied displacement increased, the bundles stretched in both in-plane (the x-y plane in Fig. 1) and out-of-plane (the x-z and y-z planes in Fig. 1) directions during testing. They exhibited diverse responses: some reoriented and stretched without breaking while others ultimately ruptured (Fig. 4). Breakages frequently coincided with displacements immediately following local maxima in the load–displacement curve. Smooth muscle bundles moved independently from the collagen fibers during loading, demonstrating a lack of structural cohesion in the USLs. The smooth muscle bundles exhibited distinct failure mechanisms, including rupture and delamination, the latter characterized by the separation of tissue layers.

The GDV for each specimen was also computed at a subset of the applied displacement (Fig. 6(b)). As seen clearly in Fig. 6(b), as

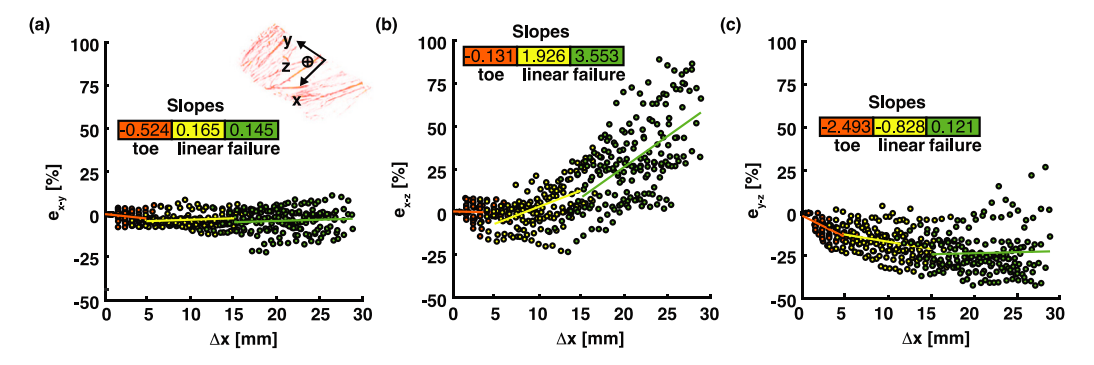


Fig. 8. BEP relative change *versus* displacement during uniaxial tensile testing in the (a) x-y plane, (b) x-z plane, and (c) y-z plane for n=14 USL specimens. Structural bundles realigned in the loading direction, the x-direction, as shown by the increasing e_{x-z} and decreasing e_{y-z} . These changes were monotonic (increasing or decreasing) during loading for nearly all USL specimens. The fiber bundles had minimal realignment in the out-of-plane direction, as demonstrated by the constant e_{x-y} . A linear fit was applied across n=14 specimens to BEP relative change *versus* displacement data within each loading region and the slopes in each region are also reported.

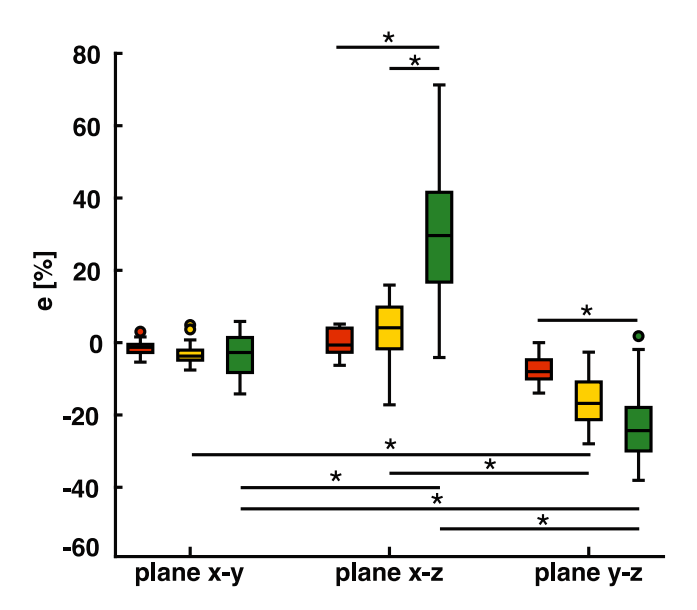


Fig. 9. Boxplot of the BEP relative changes (means across each region) in the toe (orange), linear (yellow), and failure (green) regions across the x-y, x-z, and y-z planes for n=14 USL specimens. In the x-z plane, e_{x-z} was significantly higher in the failure region compared to the linear and toe regions, indicating increased fiber realignment. In y-z plane, e_{y-z} in the failure region was significantly different from e_{y-z} in the toe region, while no regional differences were observed for e_{x-y} in the x-y plane. Furthermore, in the linear region, e_{y-z} was significantly different from both e_{x-y} and e_{x-z} , whereas in the failure region, all three BEP relative changes $(e_{x-y}, e_{x-z}, and e_{y-z})$ exhibited significant differences, emphasizing a multidirectional structural response under extreme loading conditions (*, p < 0.05).

the displacement increased, the load increased non-linearly in the toe region while the tissue GDV decreased. In the linear region, GDV remained roughly constant. In the failure region, following the maximum load, an increase in GDV was recorded as the USLs started to fail and the load gradually decreased. Slopes of lines that fit the GDV versus displacement curves in the three regions are presented in Fig. 6(b) to further illustrate the differences across the regions. A one-way ANOVA revealed a significant effect of region on mean GDV values (p = 0.0003) (Fig. 7). Post hoc pairwise comparisons indicated that the failure region had significantly different mean GDV values than the toe and linear regions (p = 0.0002). The failure of the USL specimens occurred progressively, involving numerous discrete breakages of collagen and smooth muscle bundles that collectively contributed to the overall USLs' failure. By observation, failure occurred primarily in the intermediate regions of the specimens, where OCT images were acquired (refer to Fig. 1(a)-(b)).

Fig. 8 shows the BEP relative change, e, across three orthogonal planes for n = 14 USLs. The increase in e_{x-z} and decrease in e_{y-z} indicated the realignment of bundles in the loading direction as displacement increased. The slight change in e_{x-y} indicated no significant realignment away from the ligament plane for these bundles, consistent with the planar nature of the specimens. A two-way ANOVA revealed a significant interaction between the plane and mechanical region (p < 0.0001), indicating that BEP relative changes depended on both factors (Fig. 9). In the x - z plane, e_{x-z} was significantly higher in the failure region than in the linear and toe regions, reflecting increased bundle realignment during testing. In the y-z plane, e_{y-z} in the failure region differed significantly from $e_{\nu-z}$ values in the toe region, while no regional differences were found for e_{x-y} in the x-y plane. The e_{y-z} showed significant differences from the e_{x-y} and e_{x-z} in linear region, whereas e_{x-y} , e_{x-z} , and e_{y-z} differed in the failure region, highlighting a multidirectional structural response under failure loading.

3.3. SHG microscopy

Several SHG images were obtained from n = 8 USL specimens in their three anatomical regions, the proximal, intermediate, and distal regions, before and after uniaxial tensile testing. Compared to the millimeter-scale resolution of OCT, SHG imaging captures tissue morphology at much finer, micron-scale level of detail. The images collected before loading showed rich collagen and smooth muscle content in the USLs. The collagen was mainly arranged in thick, wavy bundles and appeared to be oriented in several different directions (Fig. 10(a) and Fig. 11(a)). In the distal regions of the specimens, collagen was consistently plentiful and tortuous, but little smooth muscle was observed. In the proximal regions, collagen fibers generally appeared to be less dense and were often woven between layers of smooth muscle (Fig. 10(a) and Fig. 11(a)). The intermediate regions of the specimens contained a mixture of these features, with some smooth muscle and dense collagen fiber bundles observed (Fig. 10(a) and Fig. 11(a)). Sometimes, collagen, often in the proximal region but sometimes in the other regions, appeared to be wrapped around cylindrical, branching structures, which were likely blood vessels (e.g., see Fig. 10(a), top row, second image). Often the smooth muscle bundles were oriented diagonally between the x and y directions (Fig. 11).

The images taken after uniaxial tensile testing showed many of the same features, with the distal regions displaying wavy collagen fibers and the proximal areas containing layers of smooth muscle and collagen (Fig. 10(b) and Fig. 11(b)). As expected, discontinuities in collagen and muscle bundles were observed since the USL specimens primarily failed in the intermediate regions. Overall, the before- and after-loading SHG images appeared similar, with no significant changes in tissue morphology.

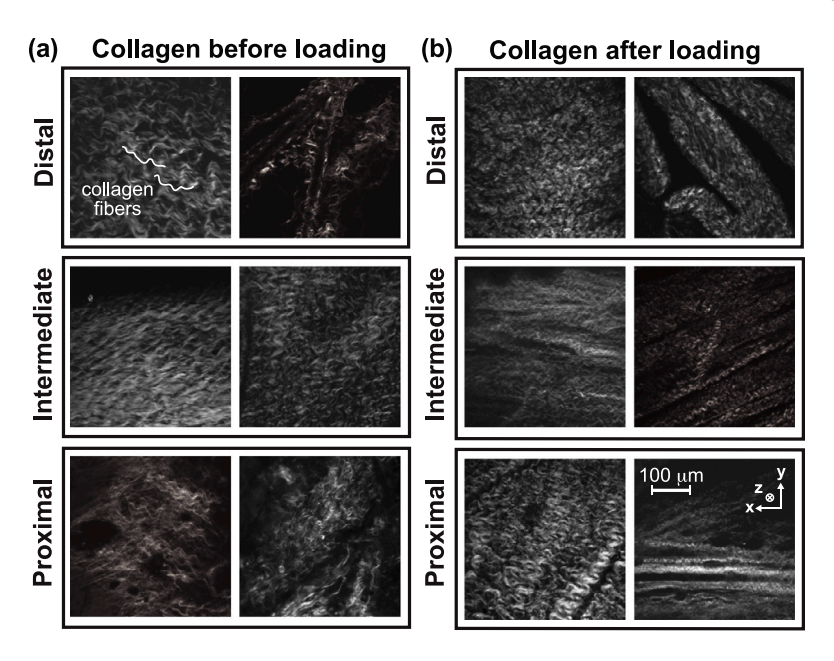


Fig. 10. SHG images of collagen (a) before and (b) after tensile testing in the distal, intermediate, and proximal regions of rat USLs. Two representative images are shown for each region.

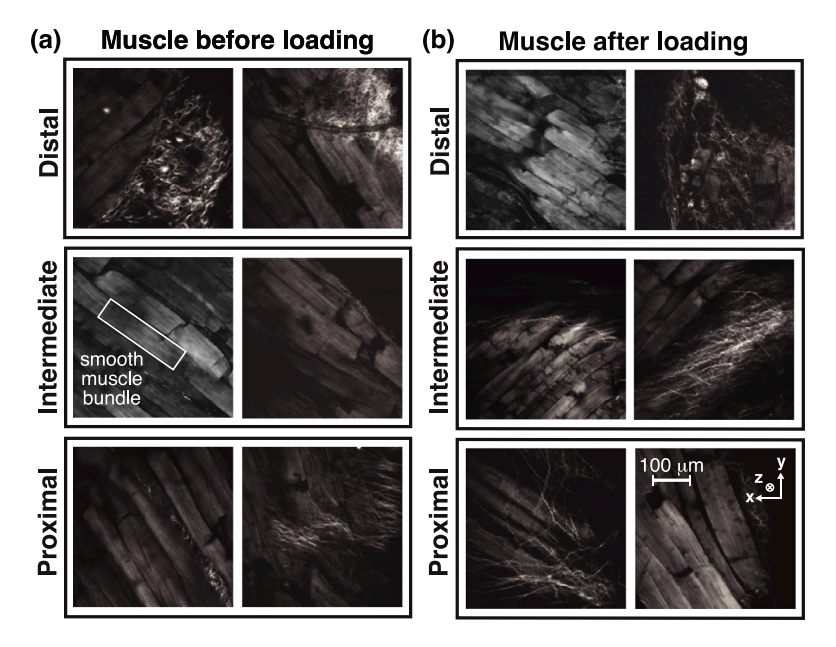


Fig. 11. SHG images of smooth muscle (a) before and (b) after tensile testing in the distal, intermediate, and proximal regions of rat USLs. Two representative images are shown for each region.

4. Discussion

In this experimental study, we explored the role that the main microstructural components of rat USLs play in their mechanical function. Using OCT imaging during uniaxial tensile testing, we visualized the contributions of collagen fiber and smooth muscle bundles to the heterogeneous mechanical behavior of these ligaments with high resolution (tens of microns). SHG microscopy, conducted before and after the uniaxial testing, provided complementary images on the organization of single collagen fibers and smooth muscle bundles within the USLs with increased resolution, reaching the micron scale. To our knowledge, this is the first study to present detailed micro-mechanical data on rat USLs using label-free imaging methods.

The load-displacement data shown in Fig. 6(a) for the tested specimens were very similar to those of rat USLs in our previous study,

where the DIC was employed to measure the strain fields [11]. Consistent with previous observations, multiple failures occurred in the intermediate region, characterized by tissue delamination and the failure of distinct bundles. Our findings showed the advantages of OCT-based imaging in characterizing the three-dimensional heterogeneous structure of the USLs under tensile loading. The depth-resolving capability of this imaging technique offered unprecedented data on the complex architecture of USLs. Integrating the OCT-derived GDV metric with load–displacement data revealed significant correlations between the structural features and the mechanical behavior of the USLs. This approach provided an understanding of the nonlinear mechanical response of the USLs, as characterized by the three distinct regions (toe, linear, and failure) of the load–displacement curve (Fig. 6). In the toe region, the monotonic decrease in GDV was associated with the straightening and alignment of collagen fiber and smooth muscle

J. Thomas et al. Acta Biomaterialia 205 (2025) 405–418

bundles, which reduces the depth differences between these structural features. In the linear region, GDV remained constant even as the specimens experienced increasing displacement. This suggests that the tissue was being stretched in a way that did not significantly change the overall internal structure. Although the tissue was elongating and becoming thinner, the spatial arrangement and depth distribution of collagen and smooth muscle remained consistent throughout the specimen. As a result, the depth variability, and thus GDV, did not change. In contrast, in the failure region, a statistically significant increase in GDV coincided with abrupt decreases in load as bundles ruptured (Fig. 6(b)). When bundles begin to break, local structural rearrangements occur: parts of the tissue shift, bundle segments may slide past each other, and the spatial arrangement of various features changes. These local disruptions increase the variability in depth across the specimen, leading to a rise in GDV. It must be noted that, in this study, GDV was computed based on MIP along the depth (the z-direction) which is the natural choice for rat USLs, given their thin structure. However, this metric does not reveal heterogeneity in other directions. GDV can also be calculated along other directions, and these additional metrics can be particularly helpful for bulk specimens with similar dimensions in all directions.

The GDV *versus* displacement data were distinct across the three regions of the load–displacement curves, with statistical differences found between the mean GDV value in the failure region compared to the toe and linear regions. These findings suggest that the OCT can be used as an imaging method for determining the integrity and support function of the USLs. Our ability to correlate GDV data with mechanical properties provides an innovative approach to addressing the limitations of current *in vivo* OCE techniques. These methods typically rely on small-scale perturbations to measure tissue properties, which limits their applicability to situations involving large tissue deformations and failure.

OCT data revealed the realignment of bundles throughout uniaxial tensile testing. Collagen and smooth muscle bundles were clearly visible in the $i_{MIP}(x, y; \Delta x)$ images but were generally more difficult to detect in the other two MIP projections, $i_{MIP}(x,z;\Delta x)$ and $i_{MIP}(y,z;\Delta x)$ (Fig. 4). This was primarily due to differences in bundle dimensions across the three directions. Due to the thin structure of the USL specimen, bundle features were best preserved in the en face MIP projection. However, as shown in Fig. 5, the BPE relative change in the other two planes still effectively quantifies bundle realignment, preserving local features even when projecting across longer distances. The BPE relative change, e, with the applied displacement Δx in each of the three planes of the USLs showed realignment consistent with uniaxial loading (Fig. 8), with e_{x-y} not changing, e_{x-z} increasing, and e_{y-z} decreasing. This means that as the USLs were pulled along their main in vivo loading direction, the network of collagen fiber bundles as well as smooth muscle bundles realigned in such direction across the thickness, with minimal realignment out of the plane of the USLs.

Direct measurement of the USL thickness was not feasible with OCT in this study due to the limited optical penetration depth of near-infrared light in soft tissue. In contrast, non-optical imaging techniques, such as ultrasound and X-ray computed tomography (CT), have deeper penetration capabilities, making them suitable for full-thickness imaging during mechanical testing to failure [47]. However, these modalities have trade-offs: ultrasound has limited spatial resolution, while X-ray CT involves higher complexity and ionizing radiation exposure. Despite its penetration limitations, OCT remains an excellent choice for imaging the USL because it provides high spatial resolution and sufficient depth penetration to capture significant structural changes.

Uniaxial tensile loading does not uniformly deform the rat USL due to its non-uniform thickness, as confirmed in our recent study quantifying strain in the proximal, mid, and distal regions [11]. The failure of rat USLs occurs through bundle realignment and delamination, complex processes that are not adequately captured by a single

thickness measurement. To better describe these structural changes, we introduced scalar quantities, such as GDV and BEP, which detail the internal microstructural reorganization within the USL during loading using tomographic data. Unlike thickness measurements, these quantities remain effective despite OCT's limited penetration depth, making them more suitable for analyzing failure mechanisms in the USL.

The DVC method has been successfully applied with OCT in previous studies to measure deformation fields [20,25,26,48]. Similarly, DIC has been utilized on rat USL specimens under uniaxial tensile loading to quantify strain fields, at least up to some loads [11]. However, both DVC and DIC assume that the deformation field is continuous, registering displacements as continuous throughout the entire image field. While this assumption holds in the toe and linear regions of the load-displacement curve, where deformations are gradual and smooth, it fails in the failure region. In this region, deformation becomes discontinuous as individual structural components, such as collagen and smooth muscle bundles, rupture. This creates a significant gap in understanding the mechanical behavior of the USL during failure, where conventional strain metrics cannot describe the underlying microstructural rearrangements. Unlike DVC or DIC, our OCT-based parameters were not limited by the assumption of continuity for the deformation field, providing a robust means of quantifying localized structural rearrangements such as bundle realignment, tissue delamination, and rupture. That said, we used global displacement, Δx , in our OCT image analysis to enable consistent comparison across specimens. While global displacement is practical, especially when localized strain tracking becomes less accurate at high deformation levels, it does not capture local strain variations resulting from thickness differences across the specimen [11], contributing to the variation observed in our data (Fig. 6).

Functional extensions of OCT, such as doppler OCT [49] and polarization-sensitive OCT [50] (PS-OCT), could offer additional methods to characterize the USLs and other pelvic tissues compromised in patients with POP. For instance, doppler OCT has been effectively used in angiography imaging of the eye's fundus to provide blood vessel image contrast along with simultaneous quantitative blood flow measurement [51]. PS-OCT has been applied for image contrast and collagen content quantification in atherosclerotic plaques from cadaveric aortas [52]. Without sacrificing endoscopic capability [53,54], these extensions to OCT could aid in characterizing the microstructure of USLs and, indirectly, their supportive function. In particular, doppler OCT could quantify blood flow for clinical evaluation of the USLs in POP patients, while PS-OCT could further facilitate micro-scale imaging that can be performed using the SHG method.

Previous histological studies of USLs have demonstrated that collagen content is significantly higher in the proximal regions compared to the markedly lower levels found in the distal regions [1,12]. In our study, we noted minimal collagen in the proximal regions of several specimens when imaging occurred before testing. However, post-test images of the USLs revealed thick, wavy bundles of collagen fibers. This change may be attributed to the reorganization of collagen fibers during tensile testing. One possible explanation for the discrepancy in collagen detection in the proximal regions is the limitations of SHG imaging. SHG has a limited penetration depth, meaning it can only effectively visualize structures within a certain distance from the tissue surface. This limitation arises because biological tissues scatter and absorb light, reducing the SHG signal as it penetrates deeper layers. In the proximal regions of rat USLs, which are much thicker than the distal and intermediate regions (on the scale of millimeters, see Table 1), the SHG signal may not have reached the deeper areas where collagen is more densely concentrated. Consequently, pre-test imaging may not have adequately captured these regions. During tensile testing, mechanical stress led to tissue delamination and the reorientation of collagen fibers, bringing some previously deeper collagen bundles closer to the surface. This structural rearrangement made these bundles visible in the post-test J. Thomas et al. Acta Biomaterialia 205 (2025) 405–418

SHG imaging, explaining why they were detectable after testing but not before.

In our SHG images, smooth muscle was frequently observed in the sacral regions and rarely in the cervical regions; human USLs are described as having a higher muscle content in the cervical region and almost none in the sacral region [1,2]. These differences may be attributed to the distinctions in quadrupedal versus bipedal anatomy. In humans, the USLs serve as the primary support structures for the apical vagina, which bears the full weight of the uterus during pregnancy. In rats, the USLs also support the vagina. However, in quadrupeds, the uterine horns extend cranially through the abdomen, and the vagina and its supporting ligaments do not bear the full increasing load of the uterus during pregnancy. Consequently, the rat vagina (and uterine horns) may require less support from the USLs and more support from other abdominal tissues, resulting in their cervical regions being thinner and having less smooth muscle content. Similar structural differences have also been noted in swine USLs [55], further supporting the impact of species-specific anatomical and functional requirements on the composition of the USLs.

Back-scattered SHG imaging, as used in this study, is subject to restricted depth penetration and reduced sensitivity to collagen fibers and smooth muscle bundles oriented parallel to the laser propagation axis. These factors may have limited our ability to fully detect structural changes within the tissue. It is also well known that collagen fibers can appear punctate in back-scattered SHG images compared to their more continuous appearance in forward-scattered SHG images, potentially impacting image interpretation [35]. Given these limitations, we have refrained from drawing definitive conclusions regarding collagen and smooth muscle arrangement and instead present our SHG-based observations as qualitative and speculative. In future studies, quantitative analysis of SHG images would be more meaningful if combined with forward-collection SHG, polarization-resolved SHG, or dual-detection systems, as these approaches provide more accurate structural information.

In our previous study on rat vaginal tissue [38], we used SHG to examine the rat vagina before and after mechanical testing, finding that collagen fibers appeared curly and disorganized in images taken before inflation testing, while post-test images showed that the collagen fibers had straightened and reoriented towards the longitudinal direction. Our SHG images of the USLs showed no discernible differences in collagen fiber waviness or orientation following tensile testing that caused tissue failure (Fig. 10). In the USLs, failure primarily occurred in the intermediate regions. Post-test imaging of the tissue remnants revealed numerous intact collagen and smooth muscle bundles, indicating that the failure, while complete in the intermediate region, did not involve a total rupture of all structural elements. Instead, the results suggest that the failure resulted from the separation and displacement of tissue layers or bundles. This interpretation is supported by OCT imaging and qualitative observations during testing, which identified inter-layer separation and bundle shifting as the main contributors to the failure mechanisms of the USLs.

The images of collagen in the USLs (Fig. 10) closely resemble SHG images of the cervical tissue to which they are connected, exhibiting abundant, curly, and disorganized collagen fiber bundles. Previous studies have documented changes in collagen waviness and organization within cervical tissue during pregnancy and menopause, reflecting alterations in mechanical function. However, no equivalent studies have been conducted for the USLs [34-36]. Mechanical studies of the USLs have demonstrated changes in their mechanical properties associated with conditions such as pregnancy, menopause, and prolapse [7,56]. Building on the methods outlined in this manuscript, future research should investigate changes in collagen and smooth muscle within the USLs that likely accompany these mechanical adaptations. Such studies could provide valuable insights into the interplay between the structure and function of the USLs, advancing our understanding of these tissues and informing treatment approaches for pelvic floor disorders.

In the present study, OCT and SHG modalities were used separately, each providing unique and valuable information at different structural scales. A more integrated approach, combining real-time mechanical data from OCT with micro-structural imaging from SHG, would enable a comprehensive, multi-scale evaluation of the USL, which is particularly important in clinically relevant contexts such as the diagnosis and monitoring of POP. Integrating fiber-level imaging with tissue-level architectural analysis could allow clinicians to better identify USL degradation, collagen remodeling, and mechanical compromise. Further refinement and integration of these techniques have the potential to improve diagnostic precision and support more effective therapeutic strategies for POP, ultimately enhancing patient outcomes and quality of life

5. Conclusions

This experimental study presents the first application of OCT and SHG imaging methods to characterize the structure of the USLs, the primary supportive tissues of the vagina, in the rat model at different resolutions. These imaging modalities were used before, during, and after uniaxial tensile in the main in vivo loading direction of the USLs. Specifically, OCT-based metrics were introduced to quantify the tissue heterogeneity and collagen and smooth muscle realignment during loading. The combined imaging and mechanical testing methods showed a gradual failure mechanism of the USLs determined by bundle failure and tissue delamination. In addition, collagen fibers and smooth muscle bundles were imaged using SHG microscopy in the proximal, intermediate, and distal regions of the USLs, showing their relative intertwined organization. These findings may guide the development of label-free imaging tools for preventing, diagnosing, and treating POP. Future studies should investigate changes in the content and organization of the USLs under various physiological and pathological conditions, potentially incorporating complementary techniques such as immunohistochemical methods and functional OCT.

CRediT authorship contribution statement

Joseph Thomas: Writing – review & editing, Writing – original draft, Visualization, Validation, Methodology, Investigation, Formal analysis, Data curation. Kandace Donaldson: Writing – review & editing, Writing – original draft, Visualization, Validation, Methodology, Investigation, Formal analysis, Data curation. Clara Gimenez: Writing – review & editing, Visualization, Validation, Data curation. Monique Vaughan: Writing – review & editing, Validation. Yizheng Zhu: Writing – review & editing, Supervision, Resources, Project administration, Methodology, Investigation, Funding acquisition, Conceptualization. Raffaella De Vita: Writing – review & editing, Writing – original draft, Visualization, Supervision, Software, Resources, Project administration, Methodology, Investigation, Funding acquisition, Formal analysis, Data curation, Conceptualization.

Funding data

Funding was provided by NSF Grant No. 1804432.

Declaration of competing interest

The authors declare that they have no known competing financial interests or personal relationships that could have appeared to influence the work reported in this paper.

Acknowledgments

Funding was provided by National Science Foundation Grant No. 1804432. Joseph Thomas gratefully acknowledges the support of the Bradley Fellowship from the Bradley Department of Electrical and Computer Engineering at Virginia Tech.

References

- R.M. Campbell, The anatomy and histology of the sacrouterine ligaments, Am. J. Obstet. Gynecol. 59 (1) (1950) 1–12.
- [2] D. Vu, B.T. Haylen, K. Tse, A. Farnsworth, Surgical anatomy of the uterosacral ligament, Int. Urogynecol. J. 21 (9) (2010) 1123–1128.
- [3] J.M. Wu, C.A. Matthews, M.M. Conover, V. Pate, M.J. Funk, Lifetime risk of stress incontinence or pelvic organ prolapse surgery, Obstet. Gynecol. 123 (6) (2014) 1201.
- [4] M.D. Barber, L. Brubaker, K.L. Burgio, H.E. Richter, I. Nygaard, A.C. Weidner, S.A. Menefee, E.S. Lukacz, P. Norton, J. Schaffer, et al., Comparison of 2 transvaginal surgical approaches and perioperative behavioral therapy for apical vaginal prolapse: the OPTIMAL randomized trial, JAMA 311 (10) (2014) 1023–1034.
- [5] K. Donaldson, J. Thomas, Y. Zhu, S. Clark-Deener, M. Alperin, R. De Vita, In-plane and out-of-plane deformations of gilt utero-sacral ligaments, J. Mech. Behav. Biomed. Mater. 131 (2022) 105249.
- [6] A. Baah-Dwomoh, J. McGuire, T. Tan, R. De Vita, Mechanical properties of female reproductive organs and supporting connective tissues: A review of the current state of knowledge, Appl. Mech. Rev. 68 (6) (2016).
- [7] K. Donaldson, A. Huntington, R. De Vita, Mechanics of uterosacral ligaments: Current knowledge, existing gaps, and future directions, Ann. Biomed. Eng. 49 (8) (2021) 1788–1804.
- [8] W. Becker, R. De Vita, Biaxial mechanical properties of swine uterosacral and cardinal ligaments, Biomech. Model. Mechanobiol. 14 (3) (2015) 549–560.
- [9] T. Tan, F.M. Davis, D.D. Gruber, J.C. Massengill, J.L. Robertson, R. De Vita, Histo-mechanical properties of the swine cardinal and uterosacral ligaments, J. Mech. Behav. Biomed. Mater. 42 (2015) 129–137.
- [10] T. Tan, N.M. Cholewa, S.W. Case, R. De Vita, Micro-structural and biaxial creep properties of the swine uterosacral–cardinal ligament complex, Ann. Biomed. Eng. 44 (11) (2016) 3225–3237.
- [11] K. Donaldson, R. De Vita, Ex vivo uniaxial tensile properties of rat utero-sacral ligaments, Ann. Biomed. Eng. (2023).
- [12] R. Iwanaga, D.J. Orlicky, J. Arnett, M.K. Guess, K.J. Hurt, K.A. Connell, Comparative histology of mouse, rat, and human pelvic ligaments, Int. Urogynecol. J. 27 (11) (2016) 1697–1704.
- [13] P.A. Moalli, N.S. Howden, J.L. Lowder, J. Navarro, K.M. Debes, S.D. Abramowitch, S.L.Y. Woo, A rat model to study the structural properties of the vagina and its supportive tissues, Am. J. Obstet. Gynecol. 192 (1) (2005) 80–88.
- [14] J.L. Lowder, K.M. Debes, D.K. Moon, N. Howden, S.D. Abramowitch, P.A. Moalli, Biomechanical adaptations of the rat vagina and supportive tissues in pregnancy to accommodate delivery, Obstet. Gynecol. 109 (1) (2007) 136–143.
- [15] B. Miller, W. Wolfe, J.L. Gentry, M.G. Grewal, C.B. Highley, R. De Vita, M.H. Vaughan, S.R. Caliari, Supramolecular fibrous hydrogel augmentation of uterosacral ligament suspension for treatment of pelvic organ prolapse, Adv. Heal. Mater. 12 (22) (2023) 2300086.
- [16] J. Brunet, B. Pierrat, J. Adrien, E. Maire, B. Lane, N. Curt, A. Bravin, N. Laroche, P. Badel, In situ visualization of aortic dissection propagation in notched rabbit aorta using synchrotron x-ray tomography, Acta Biomater. 155 (2023) 449–460.
- [17] C.M. Disney, A. Eckersley, J.C. McConnell, H. Geng, A.J. Bodey, J.A. Hoyland, P.D. Lee, M.J. Sherratt, B.K. Bay, Synchrotron tomography of intervertebral disc deformation quantified by digital volume correlation reveals microstructural influence on strain patterns, Acta Biomater. 92 (2019) 290–304.
- [18] Y. Song, D. Wu, M. Shen, L. Wang, C. Wang, Y. Cai, C. Xue, G.P.M. Cheng, Y. Zheng, Y. Wang, Measuring human corneal stromal biomechanical properties using tensile testing combined with optical coherence tomography, Front. Bioeng. Biotechnol. 10 (2022).
- [19] G. Frausto-Rea, M.H.D. l. Torre-Ibarra, R.F. Muñoz-Huerta, F.J. Casillas, Mechanical test study in composites using digital holographic interferometry and optical coherence tomography simultaneously, Appl. Opt. 59 (3) (2020) 857–865.
- [20] F. Zhong, B. Wang, J. Wei, Y. Hua, B. Wang, J. Reynaud, B. Fortune, I.A. Sigal, A high-accuracy and high-efficiency digital volume correlation method to characterize in-vivo optic nerve head biomechanics from optical coherence tomography, Acta Biomater. 143 (2022) 72–86.
- [21] C. Czerpak, M. Kashaf, B. Zimmerman, H. Quigley, T. Nguyen, The strain response to intraocular pressure decrease in the lamina cribrosa of patients with glaucoma, Ophthalmol. Glaucoma 6 (1) (2023) 11–22.
- [22] L. Wang, L. Tian, Y. Huang, Y. Huang, Y. Zheng, Assessment of corneal biomechanical properties with inflation test using optical coherence tomography, Ann. Biomed. Eng. 46 (2) (2018) 247–256.
- [23] C.L. Roberge, D.M. Kingsley, D.E. Faulkner, C.J. Sloat, L. Wang, M. Barroso, X. Intes, D.T. Corr, Non-destructive tumor aggregate morphology and viability quantification at cellular resolution, during development and in response to drug, Acta Biomater. 117 (2020) 322–334.
- [24] M. Adhi, J.S. Duker, Optical coherence tomography current and future applications, Curr. Opin. Ophthalmol. 24 (3) (2013) 213–221.
- [25] V.A. Acosta Santamaría, M.F. García, J. Molimard, S. Avril, Characterization of chemoelastic effects in arteries using digital volume correlation and optical coherence tomography, Acta Biomater. 102 (2020) 127–137.

- [26] D. Midgett, H. Quigley, T. Nguyen, In vivo characterization of the deformation of the human optic nerve head using optical coherence tomography and digital volume correlation, Acta Biomater. 96 (2019) 385–399.
- [27] H. Tran, J. Grimm, B. Wang, M. Smith, A. Gogola, S. Nelson, E. Tyler-Kabara, J. Schuman, G. Wollstein, I. Sigal, Mapping in-vivo optic nerve head strains caused by intraocular and intracranial pressures, in: Proc. SPIE, vol. 10067, 2017, p. 100670B
- [28] G. Lan, Q. Shi, Y. Wang, G. Ma, J. Cai, J. Feng, Y. Huang, B. Gu, L. An, J. Xu, J. Qin, M.D. Twa, Spatial assessment of heterogeneous tissue natural frequency using micro-force optical coherence elastography, Front. Bioeng. Biotechnol. 10 (2022).
- [29] J.H. Mason, L. Luo, Y. Reinwald, M. Taffetani, A. Hallas-Potts, C.S. Herrington, V. Srsen, C.J. Lin, I.A. Barroso, Z. Zhang, Z. Zhang, A.K. Ghag, Y. Yang, S. Waters, A.E. Haj, P.O. Bagnaninchi, Remote spatially variant debiased profiling of cell and tissue mechanical properties, 2021.
- [30] M. Marrese, N. Antonovaite, B. Nelemans, T. Smit, D. Iannuzzi, Micro-indentation and optical coherence tomography for the mechanical characterization of embryos: Experimental setup and measurements on chicken embryos, Acta Biomater. 97 (2019) 524–534.
- [31] Y.P. Huang, S.Z. Wang, S. Saarakkala, Y.P. Zheng, Quantification of stiffness change in degenerated articular cartilage using optical coherence tomography-based air-jet indentation, Connect. Tissue Res. 52 (5) (2011) 433–443.
- [32] X. Feng, G.Y. Li, A. Ramier, A.M. Eltony, S.H. Yun, In vivo stiffness measurement of epidermis, dermis, and hypodermis using broadband rayleigh-wave optical coherence elastography, Acta Biomater. 146 (2022) 295–305.
- [33] K.V. Larin, D.D. Sampson, Optical coherence elastography oct at work in tissue biomechanics [invited], Biomed. Opt. Express 8 (2) (2017) 1172–1202.
- [34] K. Myers, S. Socrate, D. Tzeranis, M. House, Changes in the biochemical constituents and morphologic appearance of the human cervical stroma during pregnancy, Eur. J. Obs. Gynecol. Reprod. Biol. 144 (Suppl 1) (2009) S82–S89.
- [35] M.L. Akins, K. Luby-Phelps, M. Mahendroo, Second harmonic generation imaging as a potential tool for staging pregnancy and predicting preterm birth, J. Biomed. Opt. 15 (2) (2010) 026020–026020.
- [36] B.F. Narice, N.H. Green, S. MacNeil, D. Anumba, Second harmonic generation microscopy reveals collagen fibres are more organised in the cervix of postmenopausal women, Reprod. Biol. Endocrinol. 14 (1) (2016) 1–8.
- [37] L. Peralta, E. Mourier, C. Richard, G. Charpigny, T. Larcher, D. Aït-Belkacem, N.K. Balla, S. Brasselet, M. Tanter, M. Muller, P. Chavatte-Palmer, In vivo evaluation of cervical stiffness evolution during induced ripening using shear wave elastography, histology and 2 photon excitation microscopy: Insight from an animal model. PLoS One 10 (8) (2015) e0133377.
- [38] J.A. McGuire, J.L. Monclova, A.C.S. Coariti, C.A. Stine, K.C. Toussaint Jr., J.M. Munson, D.A. Dillard, R. De Vita, Tear propagation in vaginal tissue under inflation, Acta Biomater. 127 (2021) 193–204.
- [39] G.L. Clark-Patterson, J.A. McGuire, L. Desrosiers, L.R. Knoepp, R. De Vita, K.S. Miller, Investigation of murine vaginal creep response to altered mechanical loads, J. Biomech. Eng. 143 (12) (2021) 121008.
- [40] Y. Zhang, M.L. Akins, K. Murari, J. Xi, M.J. Li, K. Luby-Phelps, M. Mahendroo, X. Li, A compact fiber-optic shg scanning endomicroscope and its application to visualize cervical remodeling during pregnancy, Proc. Natl. Acad. Sci. USA 109 (32) (2012) 12878–12883.
- [41] G. Ducourthial, P. Leclerc, T. Mansuryan, M. Fabert, J. Brevier, R. Habert, F. Braud, R. Batrin, C. Vever-Bizet, G. Bourg-Heckly, L. Thiberville, A. Druilhe, A. Kudlinski, F. Louradour, Development of a real-time flexible multiphoton microendoscope for label-free imaging in a live animal, Sci. Rep. 5 (1) (2015) 18303.
- [42] R. Killick, P. Fearnhead, I.A. Eckley, Optimal detection of changepoints with a linear computational cost, J. Amer. Statist. Assoc. 107 (500) (2012) 1590–1598.
- [43] A.F. Frangi, W.J. Niessen, K.L. Vincken, M.A. Viergever, Multiscale vessel enhancement filtering, in: Medical Image Computing and Computer-Assisted Intervention, MICCAI'98, Springer, 1998, pp. 130–137.
- [44] R. Ramanah, M.B. Berger, B.M. Parratte, J.O.L. DeLancey, Anatomy and histology of apical support: A literature review concerning cardinal and uterosacral ligaments, Int. Urogynecol. J. 23 (11) (2012) 1483–1494.
- [45] K.L. Sainani, Dealing with non-normal data, Pm & R 4 (12) (2012) 1001–1005.
- [46] J. Pek, O. Wong, A.C. Wong, How to address non-normality: A taxonomy of approaches, reviewed, and illustrated, Front. Psychol. 9 (2018) 2104.
- [47] J. Brunet, B. Pierrat, J. Adrien, E. Maire, B. Lane, N. Curt, A. Bravin, N. Laroche, P. Badel, In situ visualization of aortic dissection propagation in notched rabbit aorta using synchrotron x-ray tomography, Acta Biomater. 155 (2023) 449–460.
- [48] V.A. Acosta Santamaría, M. Flechas García, J. Molimard, S. Avril, Three-dimensional full-field strain measurements across a whole porcine aorta subjected to tensile loading using optical coherence tomography-digital volume correlation, Front. Mech. Eng. 4 (2018).
- [49] R. Leitgeb, C. Hitzenberger, A. Fercher, Performance of fourier domain vs time domain optical coherence tomography, Opt. Express 11 (8) (2003) 889.
- [50] J.F. de Boer, C.K. Hitzenberger, Y. Yasuno, Polarization sensitive optical coherence tomography – a review [invited], Biomed. Opt. Express 8 (3) (2017) 1838–1873.

- [51] C. Blatter, S. Coquoz, B. Grajciar, A.S.G. Singh, M. Bonesi, R.M. Werkmeister, L. Schmetterer, R.A. Leitgeb, Dove prism based rotating dual beam bidirectional doppler oct, Biomed. Opt. Express 4 (7) (2013) 1188–1203.
- [52] S.K. Nadkarni, M.C. Pierce, B.H. Park, J.F. de Boer, P. Whittaker, B.E. Bouma, J.E. Bressner, E. Halpern, S.L. Houser, G.J. Tearney, Measurement of collagen and smooth muscle cell content in atherosclerotic plaques using polarization-sensitive optical coherence tomography, J. Am. Coll. Cardiol. 49 (13) (2007) 1474–1481.
- [53] Z. Wang, H.C. Lee, O.O. Ahsen, B. Lee, W. Choi, B. Potsaid, J. Liu, V. Jayaraman, A. Cable, M.F. Kraus, K. Liang, J. Hornegger, J.G. Fujimoto, Depth-encoded allfiber swept source polarization sensitive oct, Biomed. Opt. Express 5 (9) (2014) 2931–2949.
- [54] H. Pahlevaninezhad, A.M.D. Lee, A. Ritchie, T. Shaipanich, W. Zhang, D.N. Ionescu, G. Hohert, C. MacAulay, S. Lam, P. Lane, Endoscopic doppler optical coherence tomography and autofluorescence imaging of peripheral pulmonary nodules and vasculature, Biomed. Opt. Express 6 (10) (2015) 4191–4199.
- [55] A. Baah-Dwomoh, M. Alperin, M. Cook, R. De Vita, Mechanical analysis of the uterosacral ligament: Swine vs. human, Ann. Biomed. Eng. 46 (12) (2018) 2036–2047.
- [56] C.S. Bastías, L.M. Savard, K.R. Jacobson, K.A. Connell, S. Calve, V.L. Ferguson, C.M. Luetkemeyer, Pregnancy and age differentially affect stiffness, injury susceptibility, and composition of murine uterosacral ligaments, J. Mech. Behav. Biomed. Mater. 163 (2025) 106874.